Supporting Information

The Identified Intrinsic Active Sites for Efficient and Stable Bi-functional Catalyst N-MoS_2·Ni_3S_2/NiS: Mo-N Structure and Ni-S Structure on Heterogeneous Interface Synergistically Enhance Water Splitting

Yong Gao[a], Jingjing Li[a], Hao Gong[b], Chuanxiang Zhang[c], Haiyun Fan[a], Xin Xie[a], Xianli Huang[a], Hairong Xue[a], Tao Wang[a,] *, Jianping He[a,] *

[a] College of Materials Science and Technology, Nanjing University of Aeronautics and Astronautics, Nanjing 210016, P. R. China.

[b] Department of Chemistry and Materials Science, College of Science, Nanjing Forestry University, Nanjing 210037, P. R. China.

[c] School of Materials Science and Engineering, Nanjing Institute of Technology, Nanjing 211167, China.

*Corresponding author Email: wangtao0729@nuaa.edu.cn (T. Wang); jianph@nuaa.edu.cn (J. He).

Experimental Section

1.1 Materials

All raw materials were purchased without further purification. Ammonium molybdate ($(NH_4)_6Mo_7O_{24}·4H_2O$, AR, 99%), thioacetamide (CH_3CSNH_2, AR, 99%), sodium thiosulfate ($Na_2S_2O_3·5H_2O$, AR, 99%) were purchased from Macklin Biochemical Co. Ltd. (Shanghai, China). DI water was obtained in the laboratory. And NF (1 cm × 2 cm × 0.5 mm) was obtained from commercial sources.

1.2 Synthesis of catalysts

Synthesis of N-MoS_2·Ni_3S_2/NiS: Firstly, ($(NH_4)_6Mo_7O_{24}·4H_2O$ (0.13 mmol, 0.158 g) and CH_3CSNH_2 (2.7 mmol, 0.203 g) were weighed and transferred to 30 mL DI water, and the homogeneous precursor solution was obtained by magnetic stirring for 60 minutes. Subsequently, the NF was immersed in 1.0 M HCl(aq) for 45 minutes under ultrasonic treatment to remove the surface

oxidation, then which was rinsed by DI water and ethanol, then, dried for 10 h in an vacuum oven at 60 ℃. Furthermore, after preprocessed NF was added into the above precursor solution and transferred into 50 mL Teflon-lined autoclave, hydrothermal reaction for 12 h at 180 ℃. After cooling, the catalyst was taken out and washed thoroughly in turn DI water and ethanol, then dried for 10 h in an vacuum oven at 60 ℃. Finally, the N-MoS_2·Ni_3S_2/NiS was performed electrochemical activation through three-electrode system in 1.0 M KOH(aq), importantly, the final long time electrochemical activation step was carry out before HER test is performed, not the OER test. And the loading massing of N-MoS_2·Ni_3S_2/NiS is about 4 mg·cm^{-2}. In order to investigate the effect of Mo-N bond for HER performance, several catalysts were synthesized at different hydrothermal temperature (120, 150, 180, 210 ℃) through maintaining other condition constant. In addition, the N-MoS_2·Ni_3S_2/NiS-180℃ also soaked in different concentrations H_3PO_4(aq) (0.0, 0.5, 1.0 M H_3PO_4) to further investigate the change of Mo-N bond relative rations.

Synthesis of N,Mo-Ni_3S_2/NiS and Ni_3S_2/NiS: Maintaining other conditions constant, $(NH_4)_6Mo_7O_{24}$·$4H_2O$ (0.13 mM, 0.158 g) acts as Mo and N source and $Na_2S_2O_3$·$5H_2O$ (1.35 mM, 0.338 g) acts as S source to synthesize N,Mo-Ni_3S_2/NiS, and only CH_3CSNH_2 (2.7 mM, 0.203 g) was used to synthesize Ni_3S_2/NiS.

Preparation of the Pt/C-NF and RuO_2-NF: 4 mg Pt, 1 mg carbon black and 1 mg PVDF were mixed, then adding appropriating amount of deionized water and grinding evenly, finally put into 60 ℃ oven drying to obtain Pt/C-NF. The preparation way for RuO_2-NF is as same as the Pt/C-NF.

1.3 Morphology and structure characterization

The crystal phase of N-MoS_2·Ni_3S_2/NiS and control samples were confirmed by XRD (Bruker D8 Advance) at a scanning rate of 5 °·min^{-1}. The surface morphology and hierarchical structure were

observed respectively by field emission scanning electron microscope (FE-SEM, Hitachi S-4800) and high-resolution transmission electron microscope (HR-TEM, FEI Tecnai G2F20 microscope). The thickness of N-MoS_2·Ni_3S_2/NiS was testified precisely by atomic force microscope (AFM, Bruker Multimode 8). The element chemical state and valence bond structure of N-MoS_2·Ni_3S_2/NiS and control samples were analyzed comprehensively by X-ray photoelectro spectroscopy (XPS) with a Kratos Axis Ultra DLD electron spectrometer, and all the binding energies were standardized by C 1s peak energy at 284.6 eV. The N_2 adsorption-desorption isotherms were measured at 77 K by an ASAP 2460 system to calculate the specific surface area and analyze the pore size distribution features.

1.4 Electrochemical performance characterization

All electrochemical data were collected on a CHI 760e electrochemical workstation (CHI Instruments, Inc. Shanghai, China). And the classic three-electrode system was used, including carbon rod was served as counter electrode, a SCE for HER and Hg/HgO for OER as reference electrode, and the prepared catalysts as working electrode. Linear sweep voltammetry (LSV) curves were performed at a scan rate of 5 $mV \cdot s^{-1}$ in 1.0 M KOH electrolyte with IR-compensation, the HER and OER LSV were measured respectively in N_2-/O_2-saturated electrolyte, and the CV activation was performed before LSV test. Importantly, in order to eliminate the influence of nickel oxidation peak for catalytic performance evaluation, adopting backward sweep way to collect OER LSV data. According to the Nernst equation: $E_{RHE} = E_{Hg/HgO} + 0.05916 \times pH + 0.098V$ and $E_{RHE} = E_{SCE} + 0.05916 \times pH + 0.244V$, the all potentials have been converted to RHE. The Electrochemical impedance spectroscopy (EIS) was performed with a frequency ranges from 0.01 to 100000Hz. And the ECSA was estimated through evaluating double-layer capacitance (C_{dl}), which was calculated by

different scan rate cyclic voltammetry (CV) from 20 to 100 $mV \cdot s^{-1}$ in the non-Faraday potential range. The catalyst stability was evaluated by both Accelerated Stressing Tests (AST) test in the Faraday potential range and Chronoamperometry (i-t) test at the current density of 10 $mA \cdot cm^{-2}$.

1.5 Density Functional Theory (DFT) Calculations

We adopted the Vienna Ab initio Simulation Package (VASP) to carry out all first principle Density Functional Theory (DFT) calculation, according to the generalized gradient approximation (GGA) of the Perdew-Burke-Ernzerhof (PBE) formulation [1], and the projector augmented (PAW) method [2,3]. We set the wave base cutoff to 450 eV, with a vacuum spacing of at last 15 Å perpendicular to the direction of the catalyst. And the Brillouin zone integration is performed using 3×3×1 Monkhorst-Pack k-point sampling for a structure [4]. The convergence threshold of electronic self-consistent was setas 10^{-5} eV, and the convergence threshold of geometric structure optimization was set as 0.05 eV/Å. Finally, we calculated the free energy using the following formula [5,6]:

$$G = E + ZPE - TS$$

where G, E, ZPE and TS represent respectively the free energy, total energy obtained from theoretical calculations, zero point energy and entropic contributions.

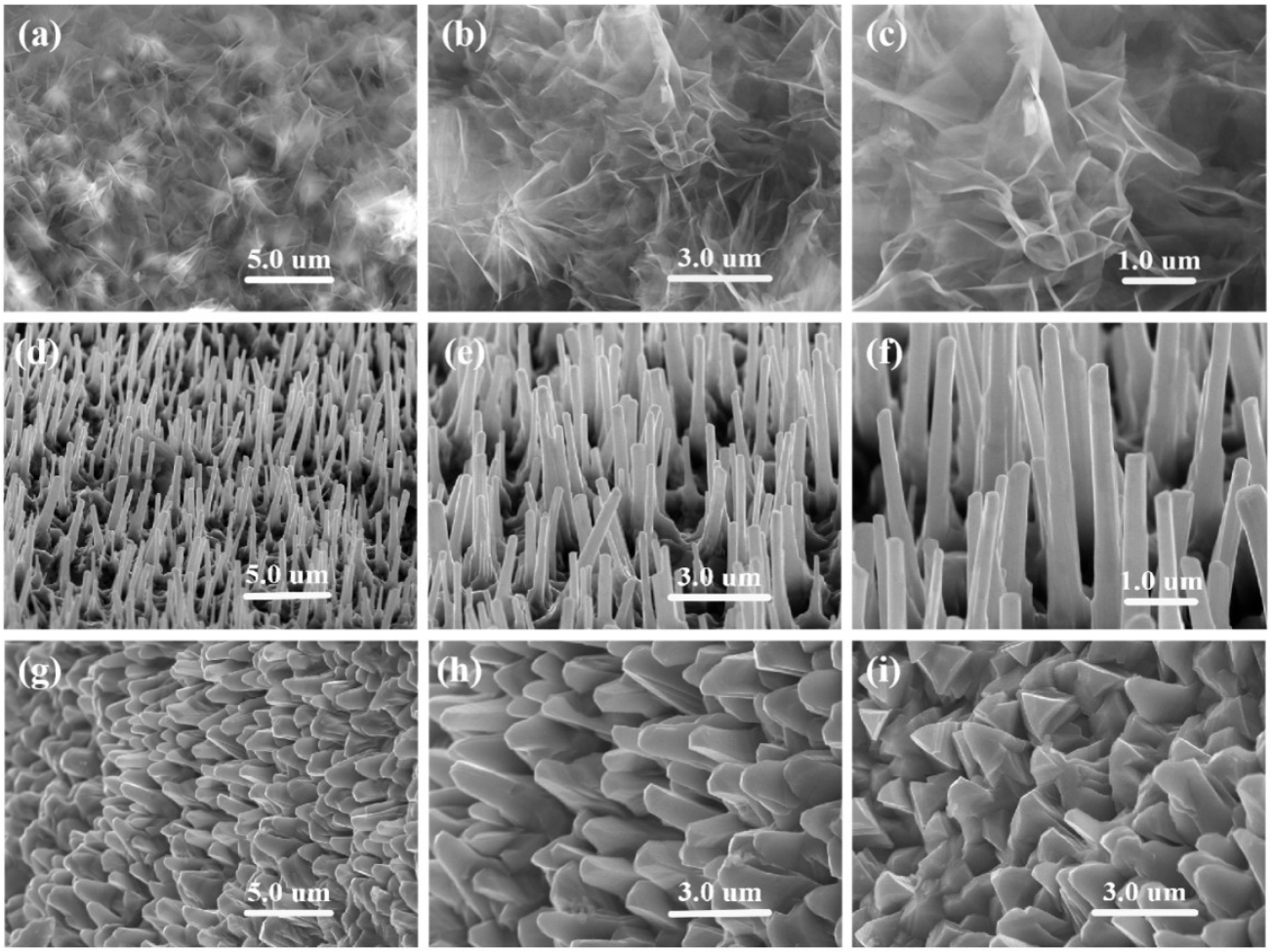

Fig. S1. The SEM images of N-MoS_2·Ni_3S_2/NiS and control samples. (a-c) N-MoS_2·Ni_3S_2/NiS, (d-f) N,Mo-Ni_3S_2/NiS, (g-i) Ni_3S_2/NiS.

The control samples N,Mo-Ni_3S_2/NiS (Fig. S1 d-f) and Ni_3S_2/NiS (Fig. S1 g-i) shows nanorod array and nanosheet array morphology. Nevertheless, the N-MoS_2·Ni_3S_2/NiS shows ultra-thin hierarchical structure with large specific surface area and electrochemical specific surface area, which could provide more active catalytic sites.

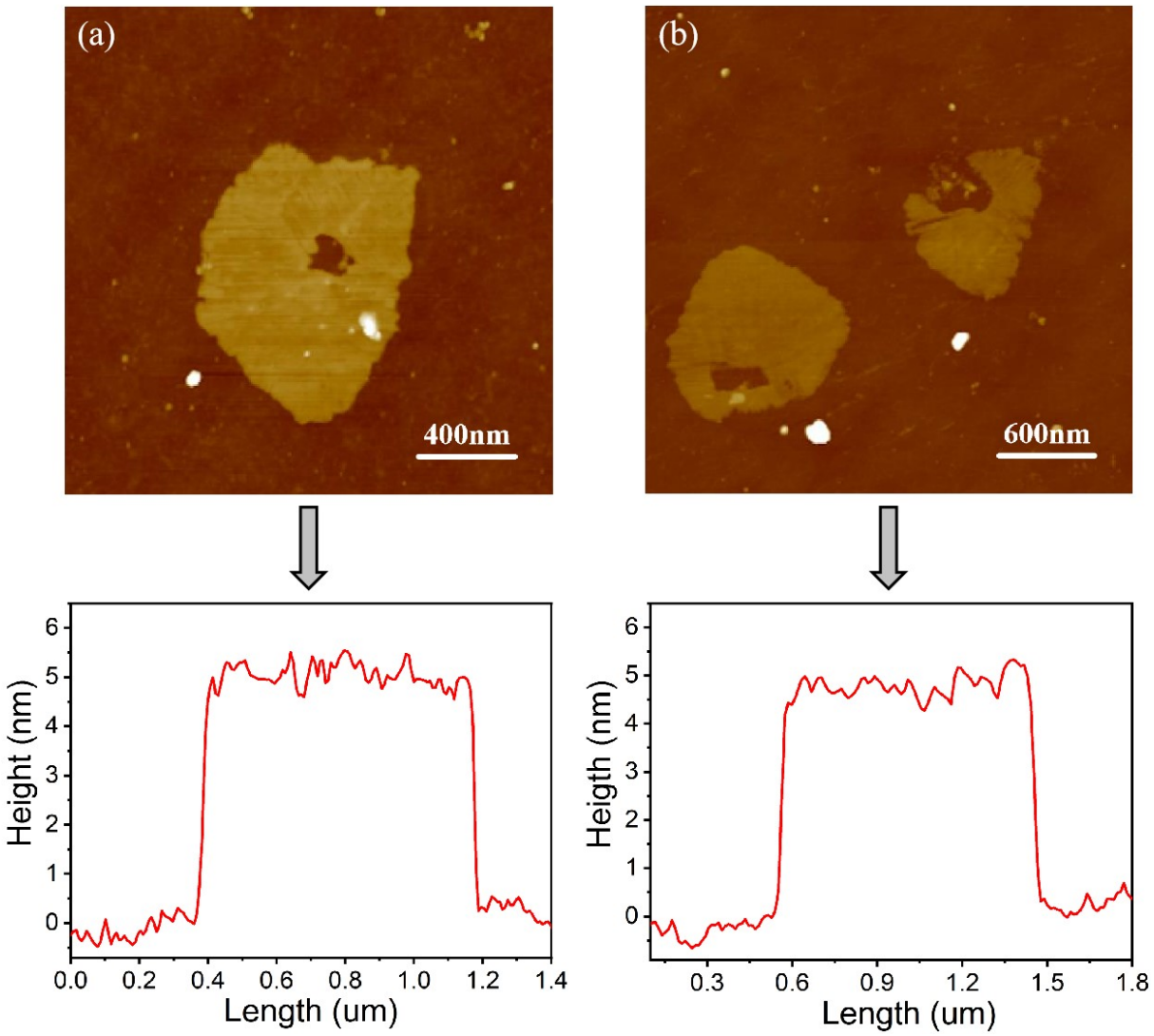

Fig. S2. AFM Height images and line-scan profiles images of N-MoS_2·Ni_3S_2/NiS.

The AFM height images reveal precisely that the average thickness is 5.2 nm for N-MoS_2·Ni_3S_2/NiS.

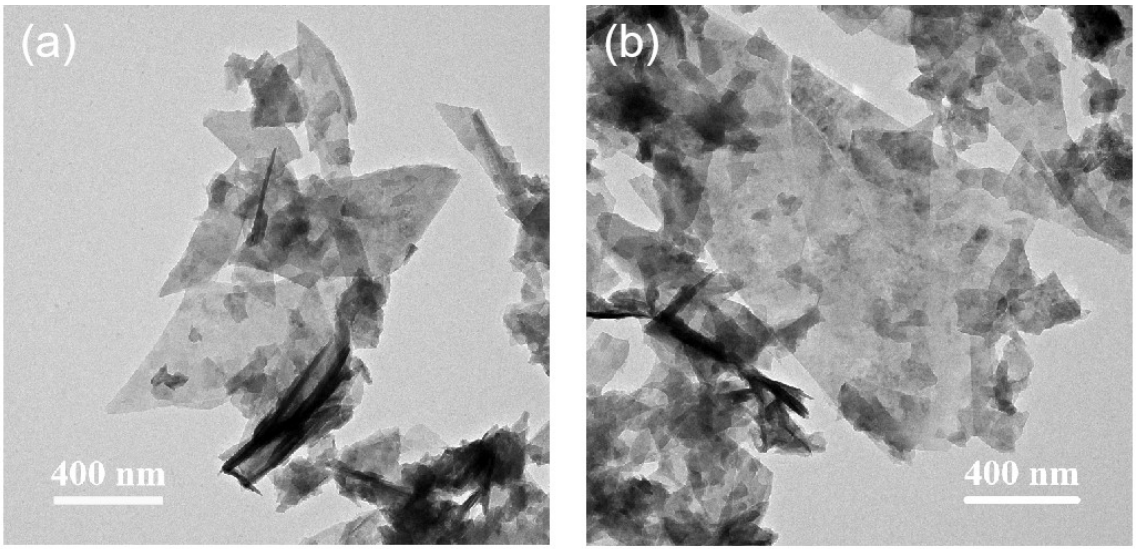

Fig. S3. (a, b) TEM images of N-MoS_2·Ni_3S_2/NiS.

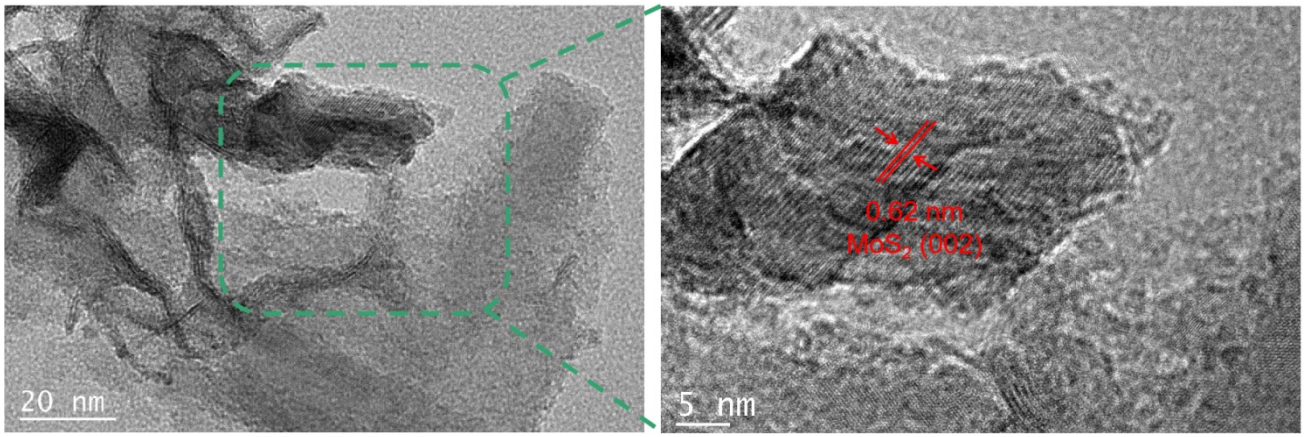

Fig. S4. The HR-TEM image of N-MoS_2·Ni_3S_2/NiS.

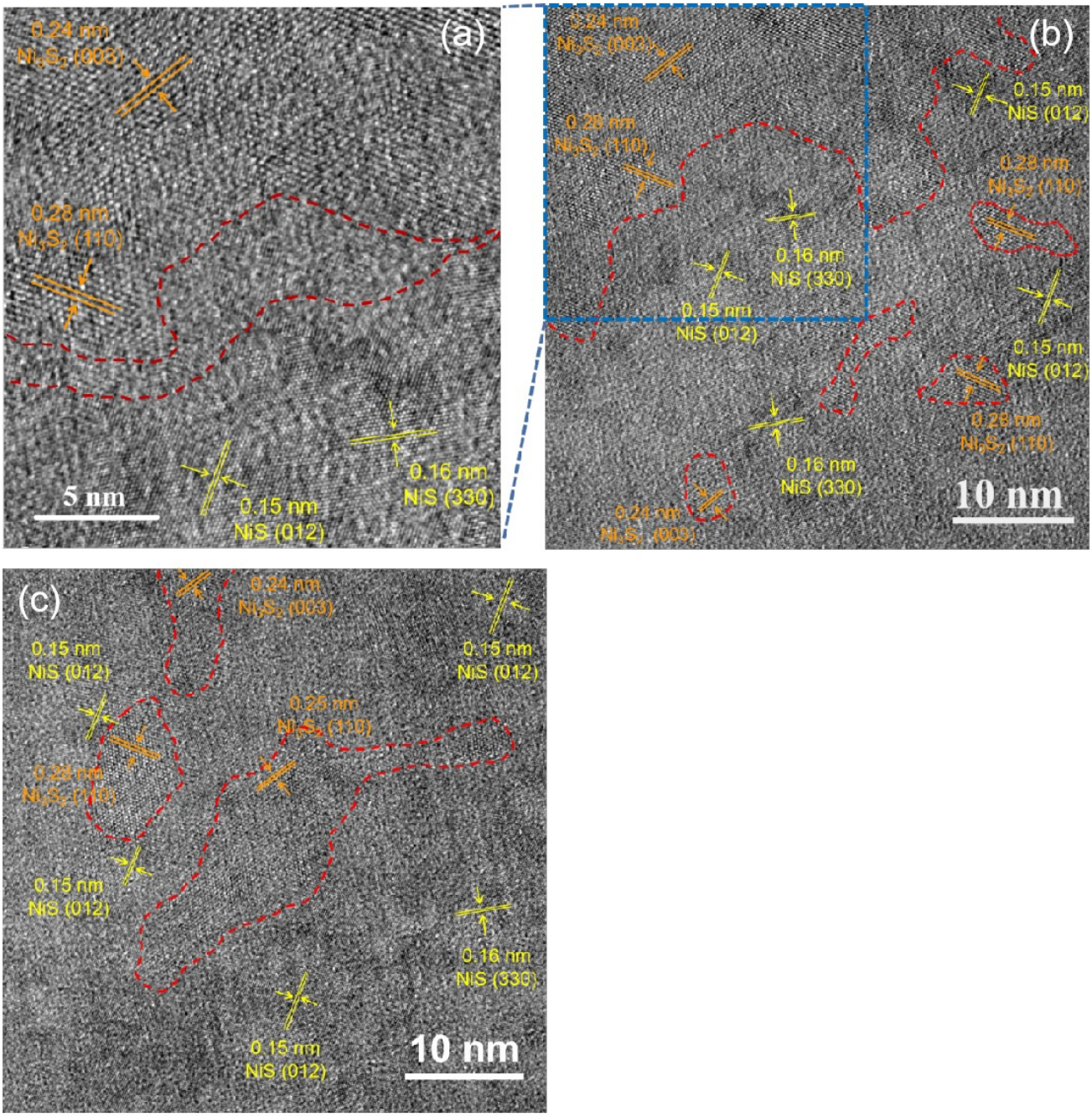

Fig. S5. HRTEM image of N-MoS_2·Ni_3S_2/NiS.

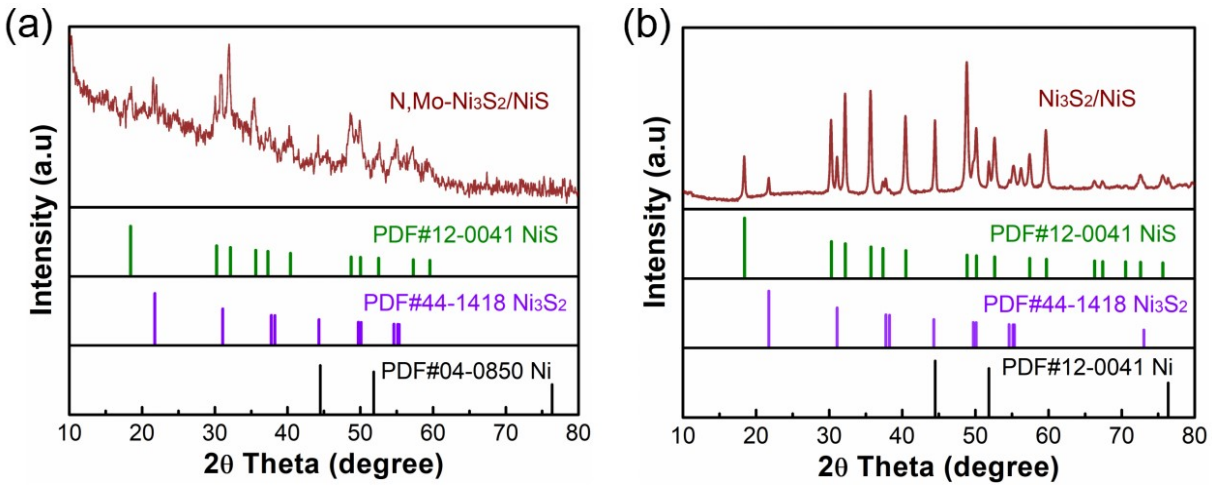

Fig. S6. XRD spectrums of (a) N,Mo-Ni_3S_2/NiS, (b) Ni_3S_2/NiS.

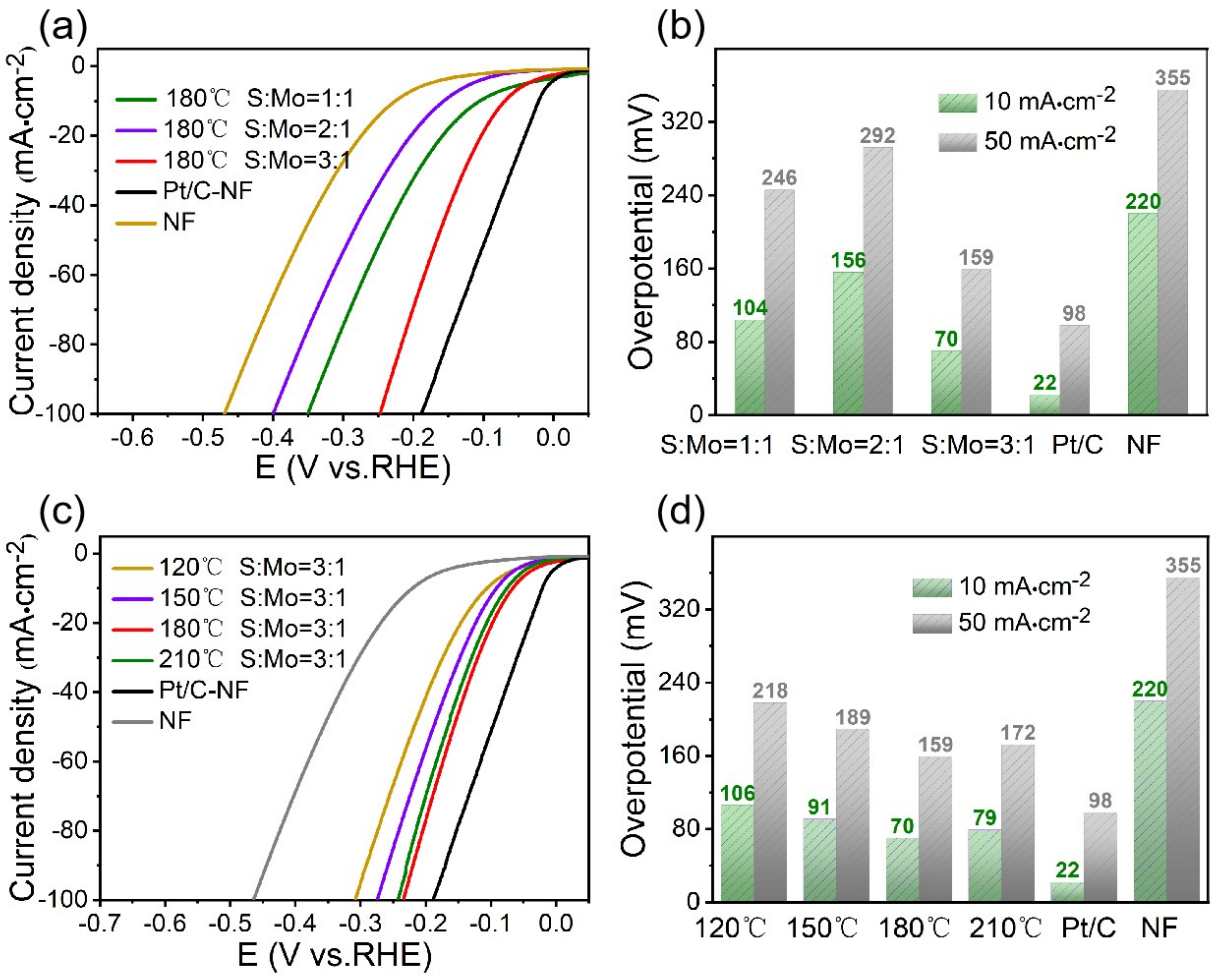

Fig. S7. (a) HER LSV curves, (b) corresponding performance plot at 10 and 50 mA·cm^{-2} of N-MoS_2·Ni_3S_2/NiS were synthesized at different temperature. (d) HER LSV curves, (e) corresponding performance plot at 10 and 50 mA·cm^{-2} N-MoS_2·Ni_3S_2/NiS were synthesized through different molar ration of S to Mo at 180℃.

Through earlier experiment exploration, the optimum N-MoS_2·Ni_3S_2/NiS was synthesized at 180℃ hydrothermal temperature when molar ration of S to Mo is 3 to 1. Meanwhile, the optimum N-MoS_2·Ni_3S_2/NiS exhibits minimum Tafel slope (95.2 mV·dec^{-1}), much lower than other samples, and only slightly higher than Pt/C-NF (54.6 mV·dec^{-1}).

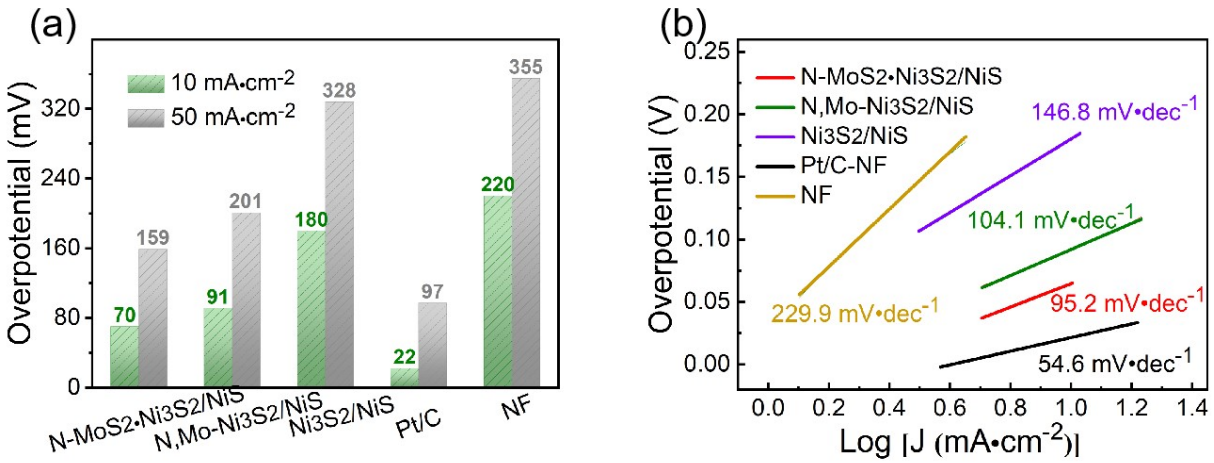

Fig. S8. (a) HER performance plot of N-MoS_2·Ni_3S_2/NiS and other control samples at 10 mA·cm^{-2} and 50 mA·cm^{-2}. (b) Corresponding Tafel slope.

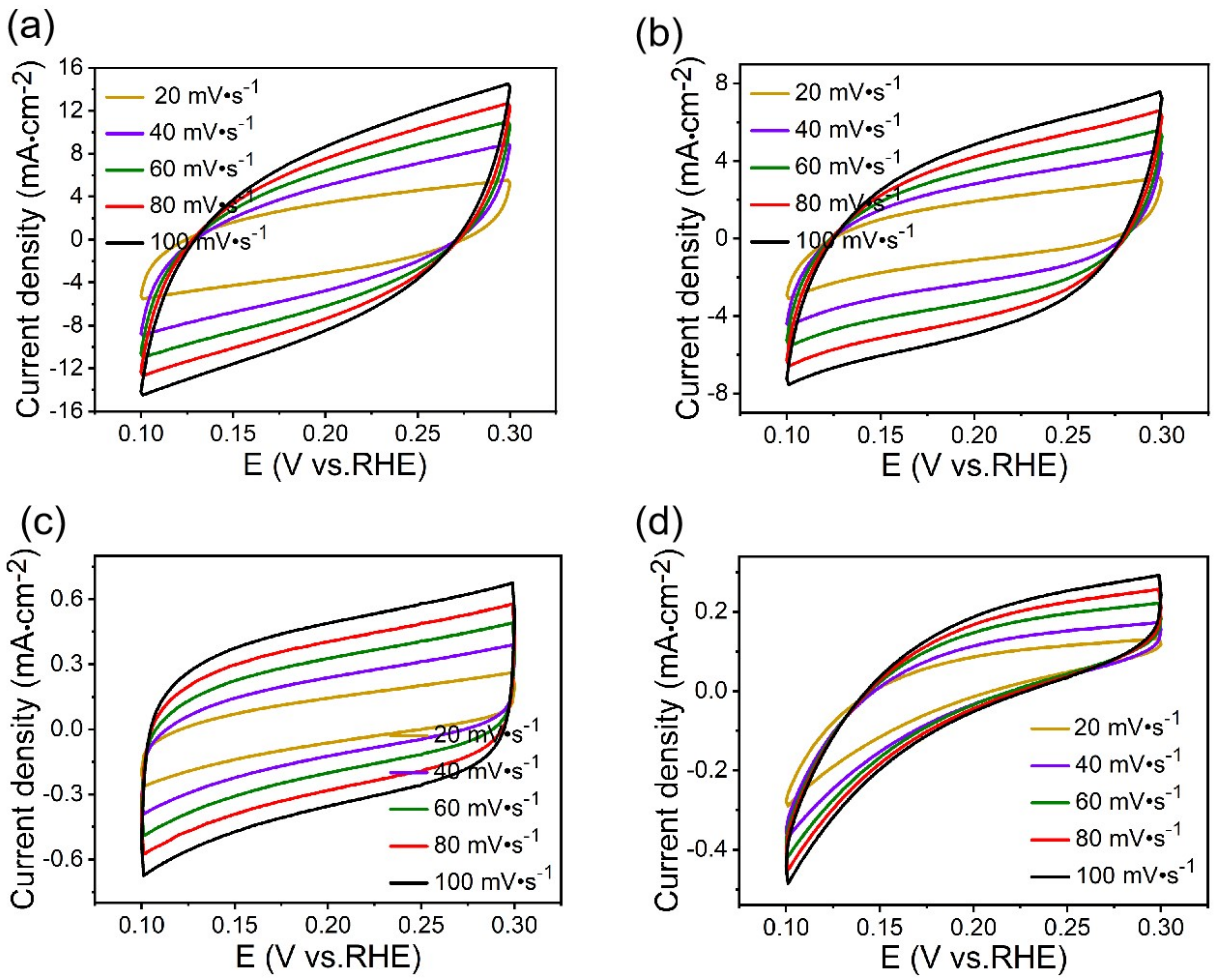

Fig. S9. HER Cyclic voltammetry of (a) N-MoS_2·Ni_3S_2/NiS, (b) N,Mo-Ni_3S_2/NiS, (c) Ni_3S_2/NiS, (d) Ni Foam at scan rate of 20, 40, 60, 80, 100 mV·s^{-1} in the potential windows of 0.1V - 0.3V (vs. RHE). (e) Corresponding the double-layer capacitance (C_{dl}).

Electrochemical specific surface area (ECSA) reflects the intrinsic activity of catalyst, which can be evaluated by C_{dl} through the equation, ECSA = Cs / C_{dl}. Herein, we adopt C_{dl} to evaluated N-MoS_2·Ni_3S_2/NiS intrinsic catalytic activity. The Cdl is 131 mF·cm^{-2} for N-MoS_2·Ni_3S_2/NiS, 83.8 mF·cm^{-2} for N,Mo-Ni_3S_2/NiS, 8.0 mF·cm^{-2} for Ni_3S_2/NiS, and 2.1 mF·cm^{-2} for Ni Foam.

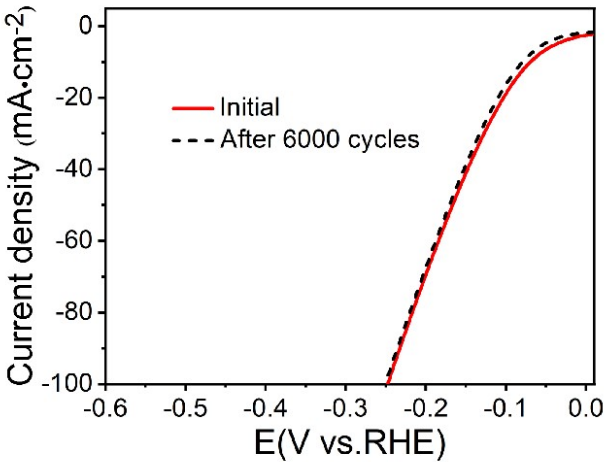

Fig. S10. HER LSV curves of N-MoS_2·Ni_3S_2/NiS before and after 6000 CVs.

MoS_2·Ni_3S_2/NiS-180℃ exhibits outstanding stability, HER performance was no decayed after 6000 CVs at 10 mA·cm^{-2}.

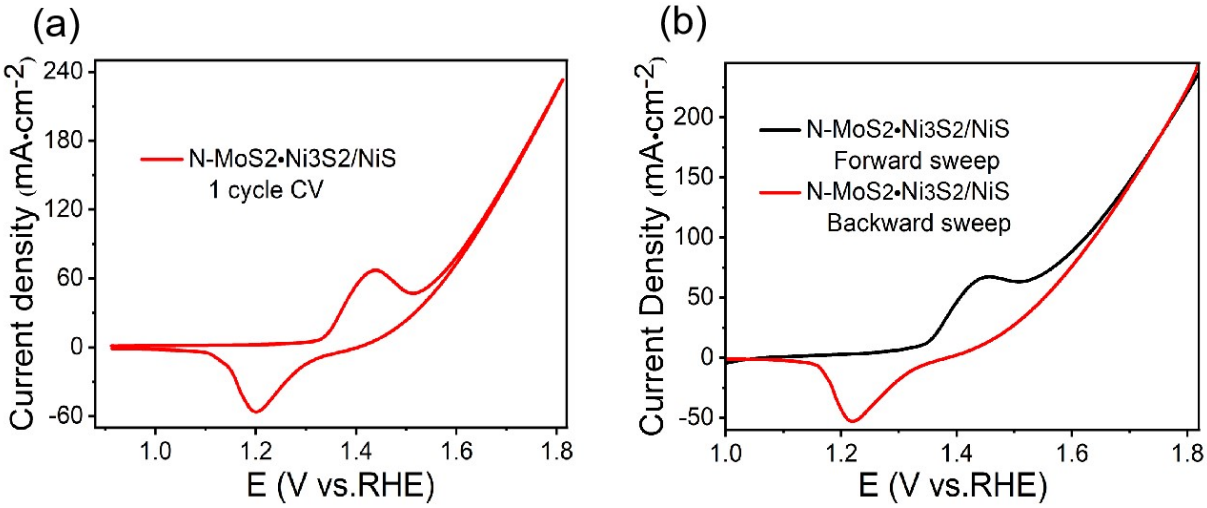

Fig. S11. (a) CV curve, (b) Forward/backward sweep OER LSV curve of N-MoS_2·Ni_3S_2/NiS.

From **Fig. S10**, the same characteristics appears in CV curve and LSV polarization curves. Which shows LSV polarization curve collected through backward sweep not only eliminate nickel oxidation peaks influence, but also evaluate well OER performance of N-MoS_2·Ni_3S_2/NiS.

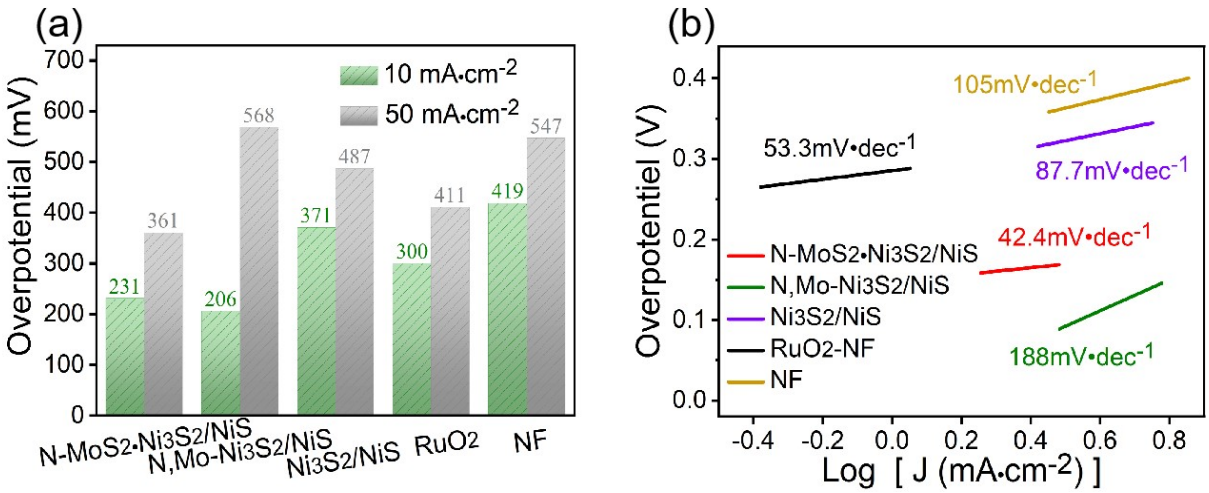

Fig. S12. (a) OER performance plot of N-MoS_2·Ni_3S_2/NiS and other control samples at 10 and 50 mA·cm^{-2}. (b) Corresponding Tafel slope.

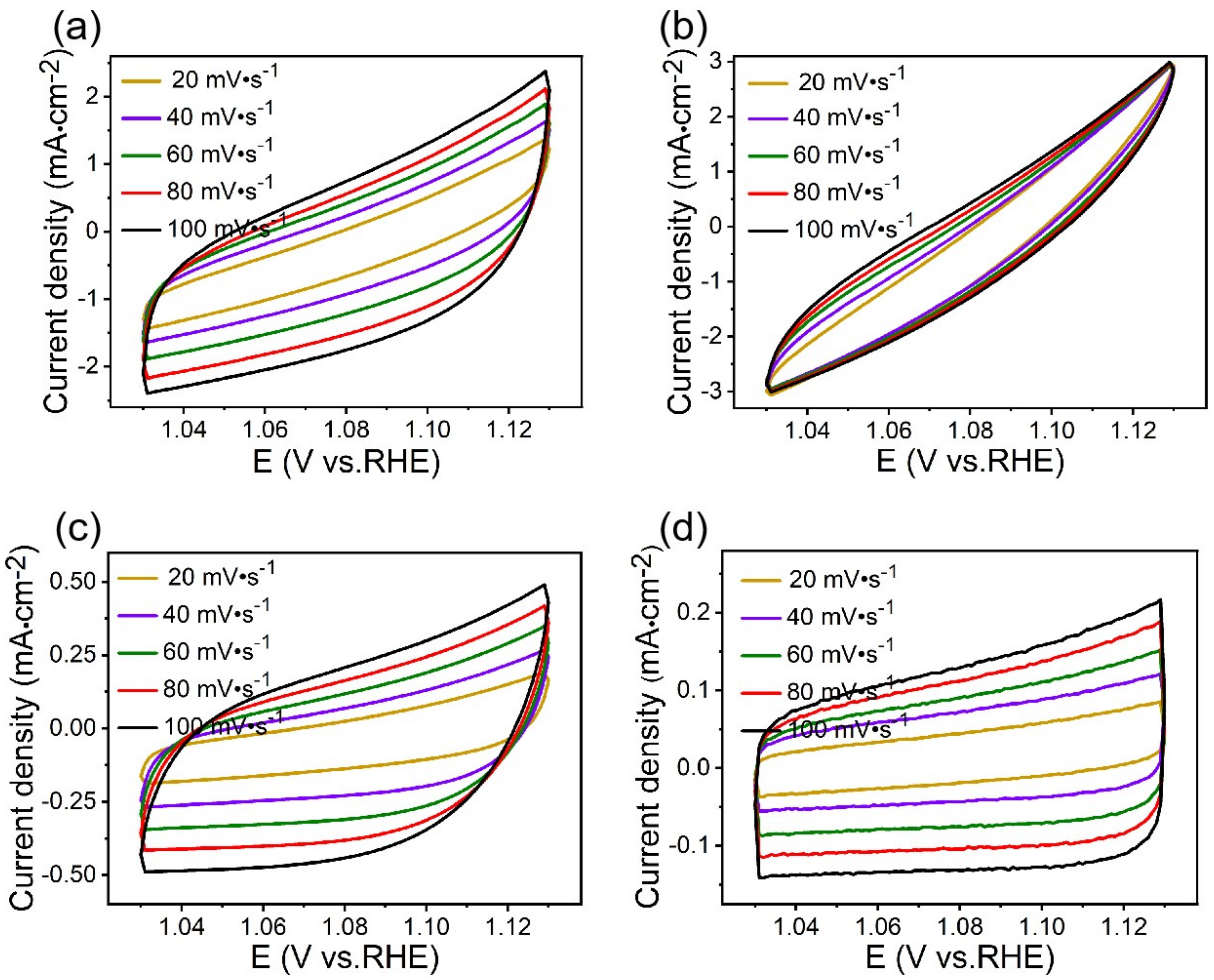

Fig. S13. OER Cyclic voltammetry of (a) N-MoS_2·Ni_3S_2/NiS, (b) N,Mo-Ni_3S_2/NiS, (c) Ni_3S_2/NiS, (d) Ni Foam at scan rate of 20, 40, 60, 80, 100 mV·s^{-1} in the potential windows of 1.03V - 1.13V (vs. RHE). (e) Corresponding the double-layer capacitance (C_{dl}).

The C_{dl} is 22.6 mF·cm^{-2} for N-MoS_2·Ni_3S_2/NiS, 9.3 mF·cm^{-2} for N,Mo-Ni_3S_2/NiS, 6.2 mF·cm^{-2} for Ni_3S_2/NiS, and 2.5 mF·cm^{-2} for Ni Foam. The value of N-MoS_2·Ni_3S_2/NiS is about 2.4, 3.6 and 9.1 times higher than N,Mo-Ni_3S_2/NiS, Ni_3S_2/NiS and Ni Foam, respectively.

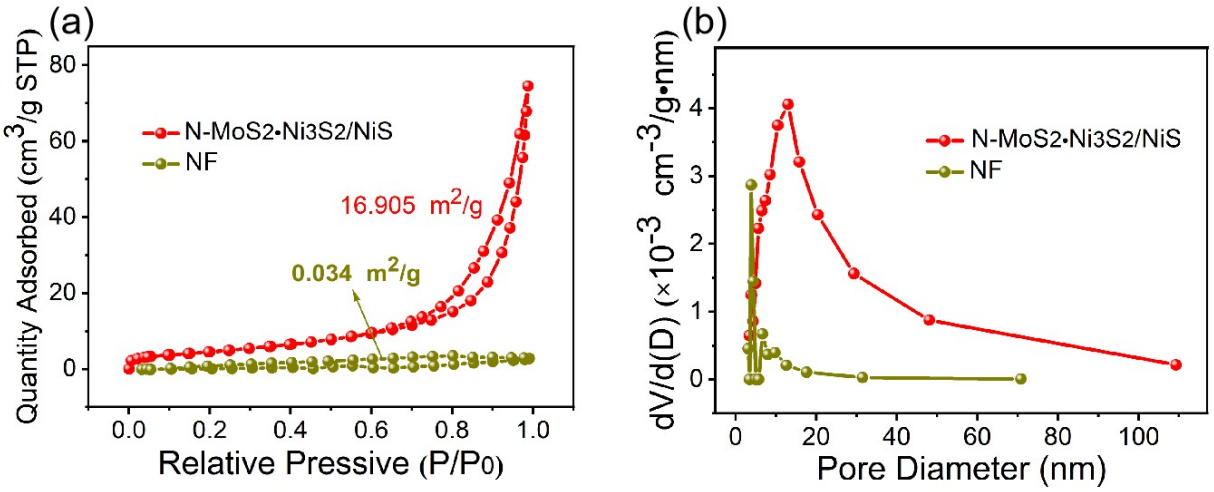

Fig. S14. (a) BET specific surface area of N-MoS_2·Ni_3S_2/NiS, NF. (b) Mesoporous pore size distribution plot of N-MoS_2·Ni_3S_2/NiS, NF.

The specific surface area of N-MoS_2·Ni_3S_2/NiS (16.905 m^2/g) is 497 times higher than NF (0.034 m^2/g), consistent with continuous ultra-thin hierarchical morphology. And mesoporous pore size is primarily concentrate on 15 nm. The BET results with C_{dl} together show N-MoS_2·Ni_3S_2/NiS has larger specific surface area and electrochemical specific surface area to load more active sites, to further improve oxygen evolution reaction performance.

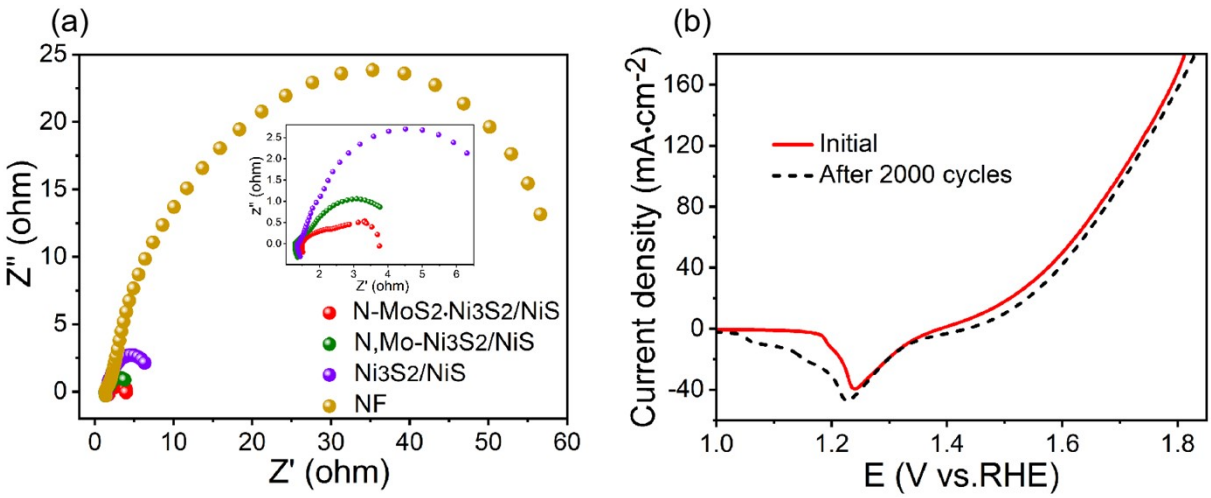

Fig. 15. (a) EIS curves of N-MoS_2·Ni_3S_2/NiS, N,Mo-Ni_3S_2/NiS, Ni_3S_2/NiS and NF at 10 mA·cm^{-2} for OER. (b) OER LSV curves before and after 2000 cycles of CV.

The N-MoS_2·Ni_3S_2/NiS has the smallest radius in **Fig. S14**a indicating that it has the smallest impedance, compared to other control samples

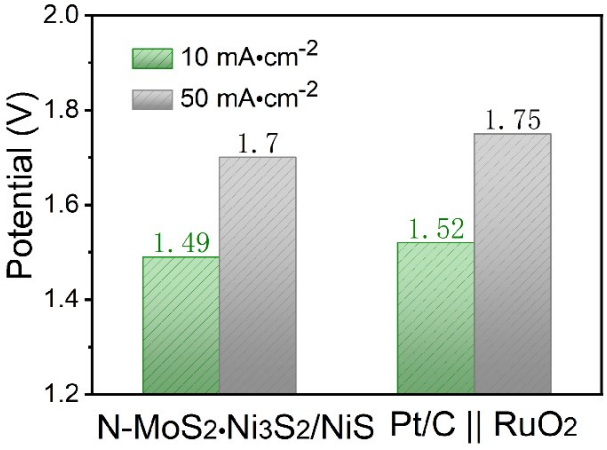

Fig. S16. The overall water splitting overpotential of N-MoS_2·Ni_3S_2/NiS||N-MoS_2·Ni_3S_2/NiS and Pt/C||RuO_2 at 10 mA·cm^{-2} and 50 mA·cm^{-2}.

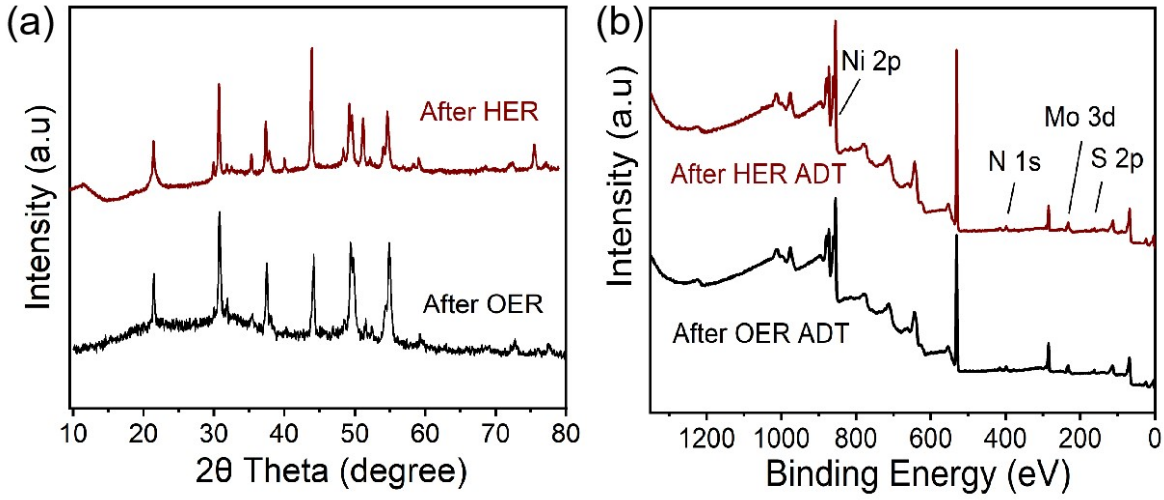

Fig. S17. (a) The XRD spectrum, and (b) the XPS spectrum for N-MoS_2·Ni_3S_2/NiS after HER and OER stability test.

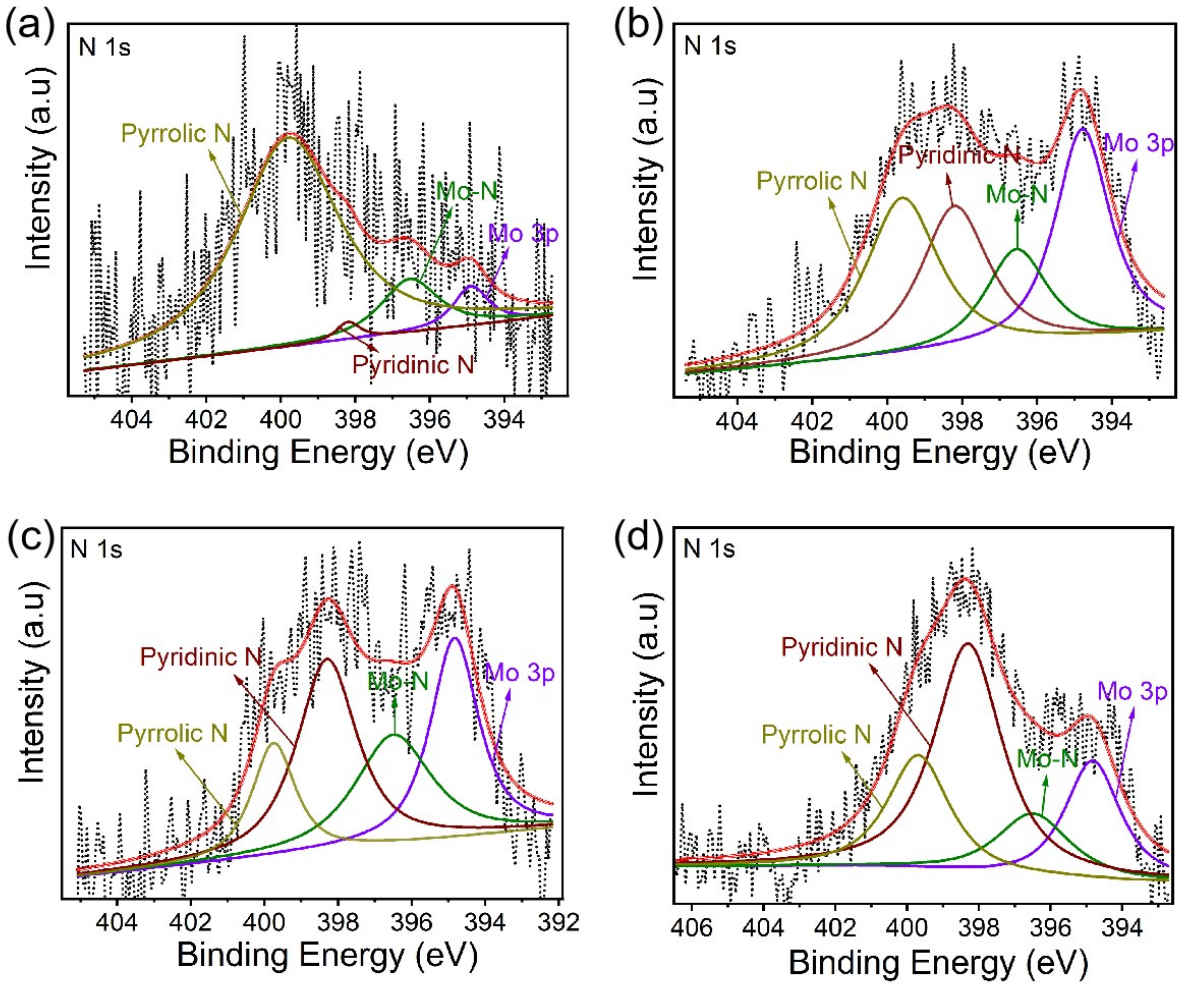

Fig. S18. The N 1s XPS spectrum of N-MoS_2·Ni_3S_2/NiS were prepared at (a) 120℃, (b) 150℃, (c) 180℃, (d) 210℃.

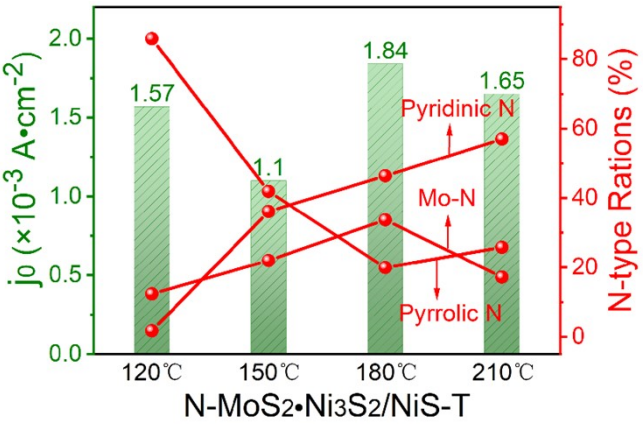

Fig. S19. The plot of exchange current density (j_0) with respect to N-type rations (%).

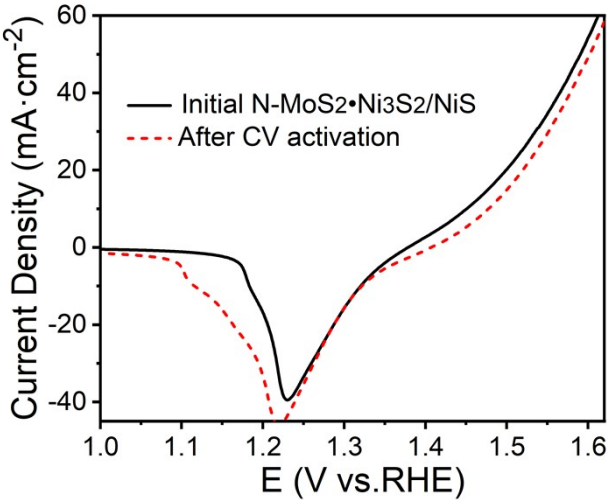

Fig. S20. The OER LSV polarization curves of N-MoS_2·Ni_3S_2/NiS befor and after CV activation.

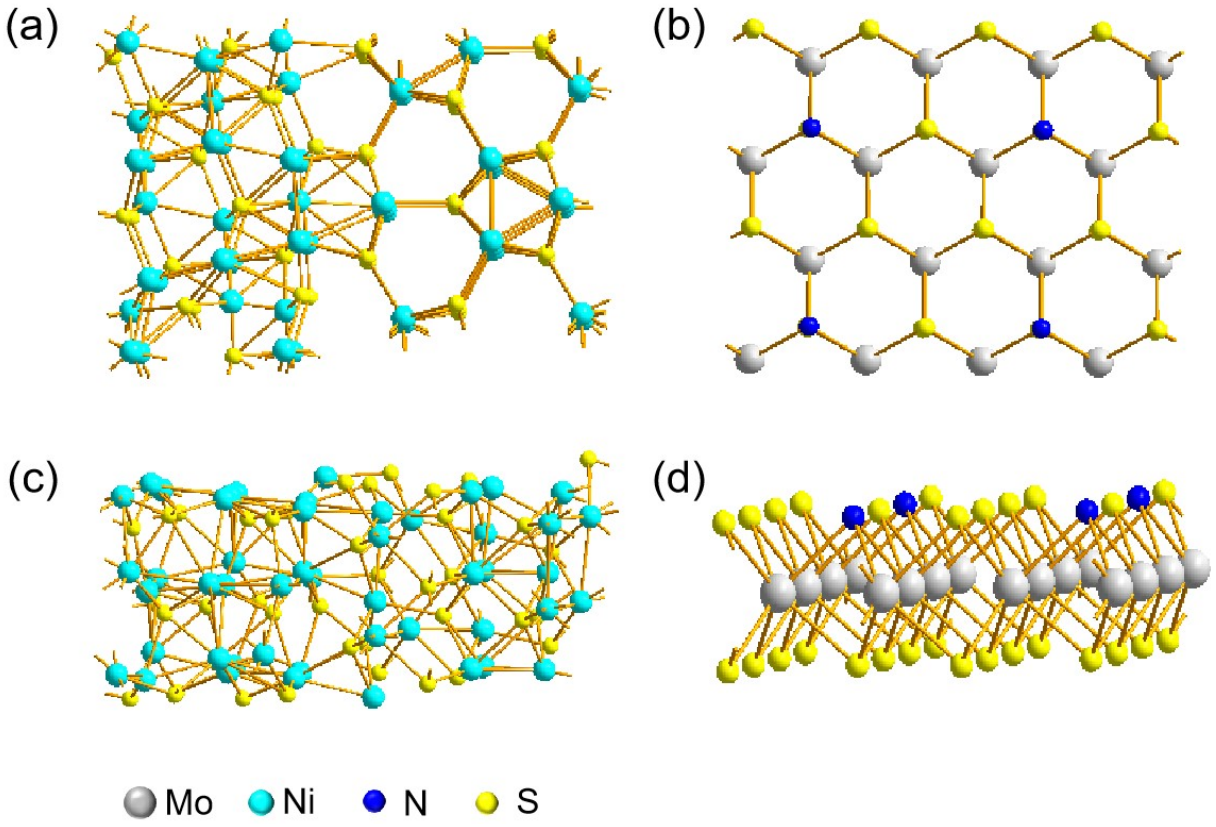

Fig. S21. Structual model diagram from different perspectives. Top view of (a) Ni_3S_2/NiS, and (b) N-MoS_2. Side view of (c) Ni_3S_2/NiS, and (d) N-MoS_2.

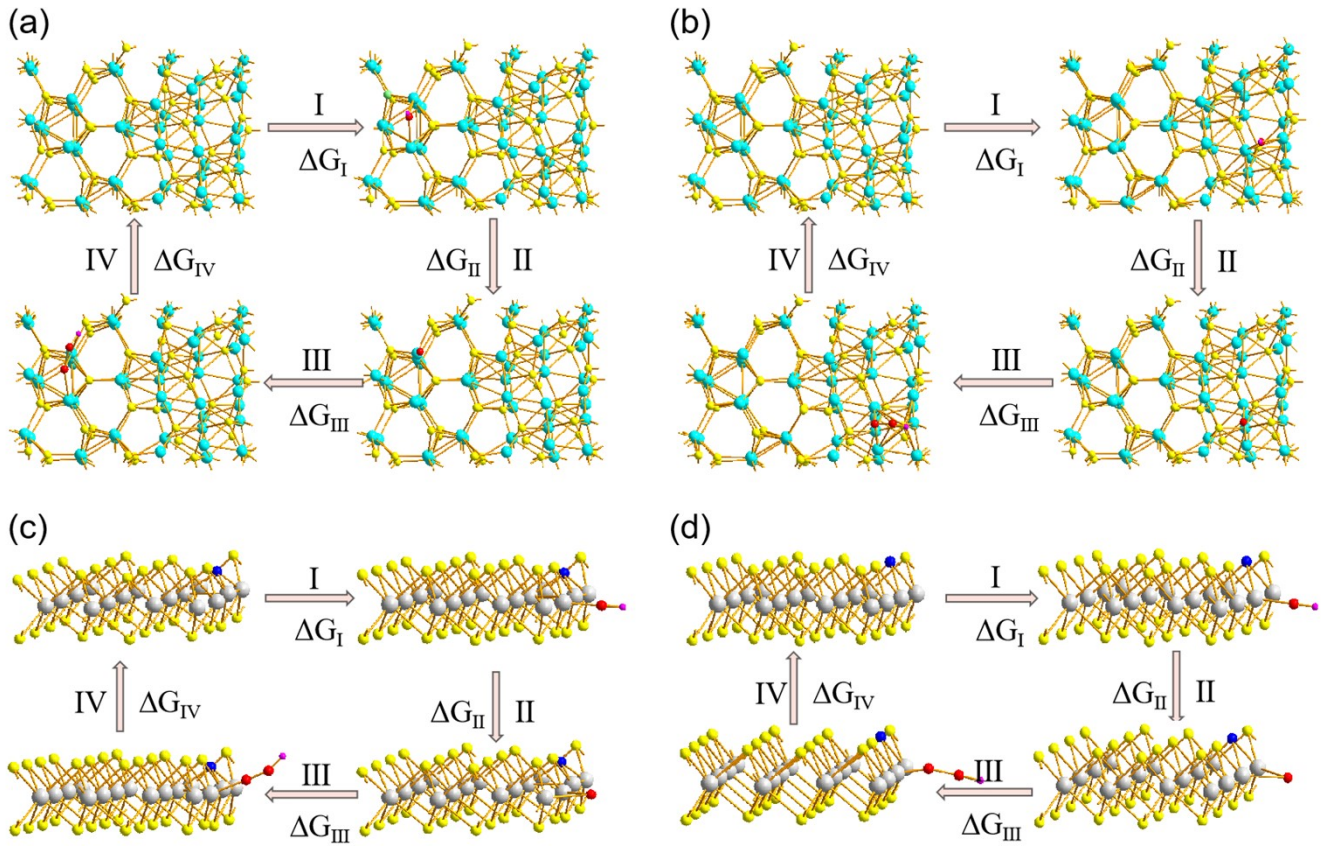

Fig. 22. The OER 4e- process of (a) NiS side, (b) Ni_3S_2 side, (c) Mo-S site and (d) Mo-N site.

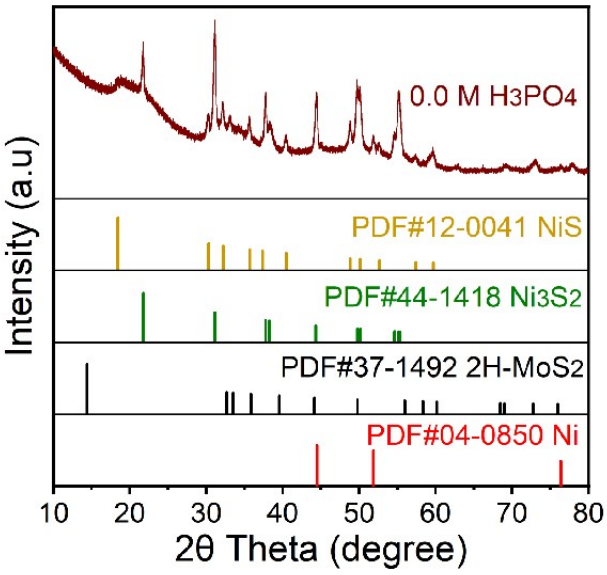

Fig. S23. XRD spectrum of N-MoS_2·Ni_3S_2/NiS immersed in 0.0 M H3PO4.

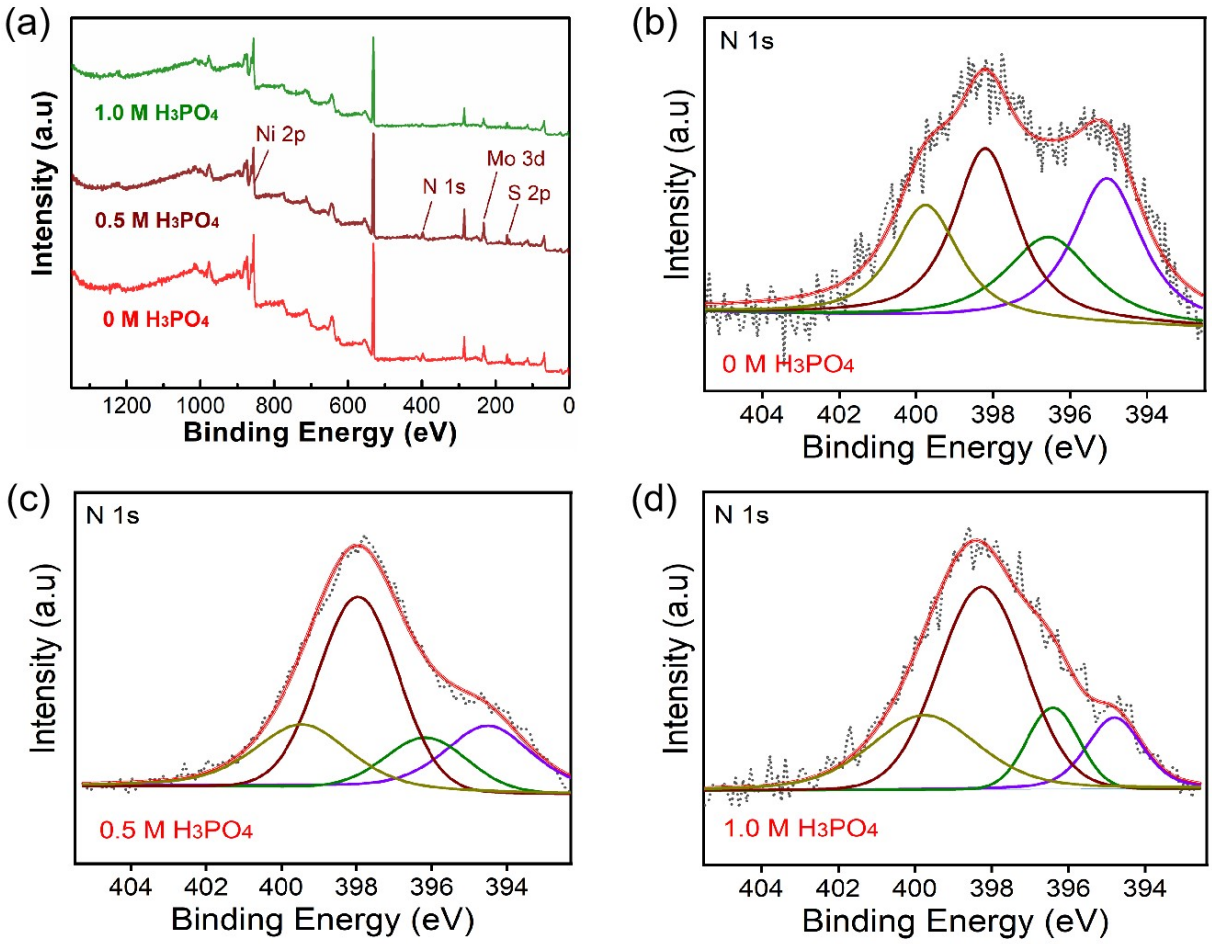

Fig. S24. The N 1s XPS spectrum of N-MoS_2·Ni_3S_2/NiS were immersed in (a) 0.0 M, (b) 0.5 M, (c) 1.0 M H_3PO_4 for 13 h, respectively.

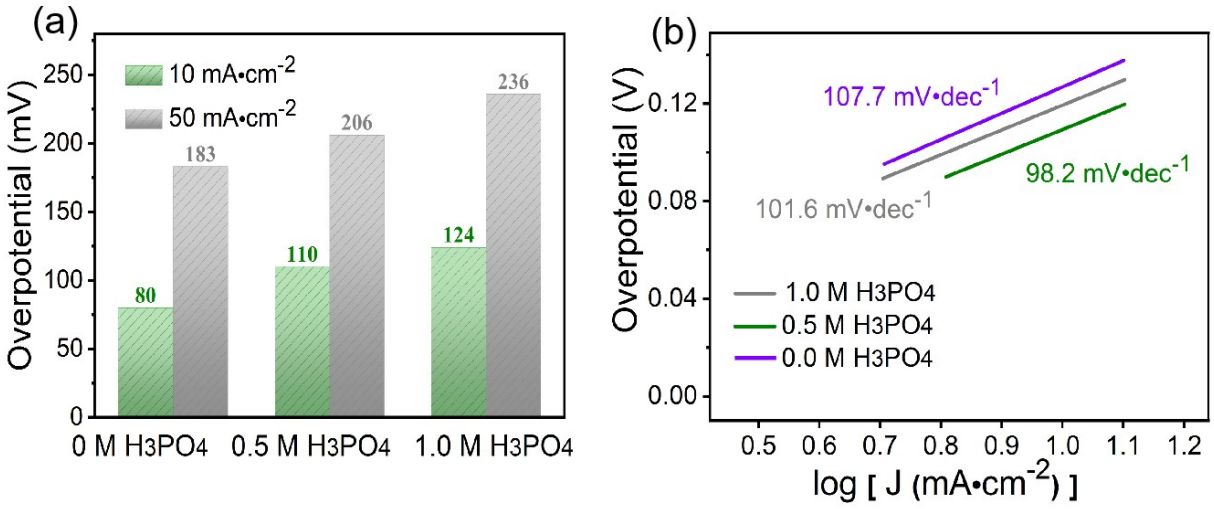

Fig. S25. (a) The HER overpotential of N-MoS_2·Ni_3S_2/NiS immersed in different concentration H_3PO_4(aq) for 13 h at room temperature. (b) Corresponding Tafel slope.

Table S1. Total N content and different N-type relative rations for N-MoS_2·Ni_3S_2/NiS were synthesized at 120, 150, 180, 210℃, respectively.

Catalyst	Total N content	Different N-type relative rations		
		Mo-N bond	Pyridinic N	Pyrrolic N
N-MoS_2·Ni_3S_2/NiS-120℃	4.49%	12.35%	1.72%	85.93%
N-MoS_2·Ni_3S_2/NiS-150℃	3.94%	21.97%	36.12%	41.91%
N-MoS_2·Ni_3S_2/NiS-180℃	3.60%	**33.69%**	46.38%	19.93%
N-MoS_2·Ni_3S_2/NiS-210℃	3.18%	17.19%	57%	25.81%

The best HER performance (70 mV@10 mA·cm^{-2}) corresponds to the highest relative rations of Mo-N bond (33.69%) when N-MoS_2·Ni_3S_2/NiS was synthesized at 180℃.

Table S2. Total N content and different N-type relative rations for N-MoS_2·Ni_3S_2/NiS that were soaked in different concentrations H_3PO_4(aq) for 13 h.

Catalyst	Total N content	Different N-type relative rations		
		Mo-N structure	Pyridinic N	Pyrrolic N
N-MoS_2·Ni_3S_2/NiS-0 M H_3PO_4	3.80%	**32.42%**	40.38%	27.20%
N-MoS_2·Ni_3S_2/NiS-0.5 M H_3PO_4	3.49%	17.16%	56.39%	26.45%
N-MoS_2·Ni_3S_2/NiS-1.0 M H_3PO_4	3.15%	13.47%	57.06%	29.47%

Table S3. The Gibbs free energy changes of each reaction step and η_{OER} in the OER 4e$^-$ process for different active catalytic sites of N-MoS_2 and Ni_3S_2/NiS.

Active catalytic site	**ΔG_I (eV)**	**ΔG_{II} (eV)**	**ΔG_{III} (eV)**	**ΔG_{IV} (eV)**	**η_{OER}(V)**
Mo-N site of N-MoS_2	0.273	-0.049	3.074	1.621	1.844
Mo-S site of N-MoS_2	-0.055	-0.056	3.425	1.606	2.195
NiS side of Ni_3S_2/NiS	0.427	0.465	2.787	1.241	1.557
Heterogeneous interface of Ni_3S_2/NiS	0.028	1.482	1.728	1.681	0.498
Ni_3S_2 side of Ni_3S_2/NiS	0.465	1.205	1.39	1.857	0.628

The OER 4e$^-$ procss reaction step：

$$* + H_2O \rightarrow OH^* + (H^+ + e^-) \qquad \Delta G_{\mathrm{I}}$$

$$OH^* \rightarrow O^* + (H^+ + e^-) \qquad \Delta G_{\mathrm{II}}$$

$$O^* + H_2O \rightarrow OOH^* + (H^* + e^-) \qquad \Delta G_{\mathrm{III}}$$

$$OOH^* \rightarrow * + O_2 + (H^+ + e^-) \qquad \Delta G_{\mathrm{IV}}$$

Table S4. The HER, OER, and water splitting performance comparison between our catalyst N-MoS_2·Ni_3S_2/NiS and reported recently Mo-/Ni-based catalysts.

Catalyst	η_{10} of HER (mV)	η_{10} of OER (mV)	η_{10} of overall water splitting (V)	Reference
N-MoS_2·Ni_3S_2/NiS	70	232	**1.4**	**This work**
MoS_2-AB/NF	77	243	1.51	[7]
Ni_2P-nanoparticle/Ni_2P-nanosheet	116	--	1.63	[8]
N-$NiMoO_4$/NiS_2	99	283	1.60	[9]
Mo-doped Ni_2P	81	270	1.54	[10]
FeNi-Mo_2C/CF	81	228	1.53	[11]
Ni/$Ni(OH)_2$	77	270	1.59	[12]
$NiS_{0.5}Se_{0.5}$	70	257	1.55	[13]
MoS_2-Ni_3S_2 HNRs/NF	98	249	1.50	[14]
FeCoMoS@NG	137	238	1.58	[15]
Fe-MoS_2/$CoMo_2S_4$	122	290	1.62	[16]
MoS_2-NiS_2/NGF	172	370	1.64	[17]

Reference

[1] J. P. Perdew, K. Burke, M. Ernzerhof, Phys. Rev. Lett. 77 (1996) 3865-3868.

[2] G. Kresse, D. Joubert, Phys. Rev. B 59 (1999) 1758-1775.

[3] P. E. Blöchl, Phys. Rev. B 50 (1994) 17953−17979.

[4] D. J. Chadi, Phys. Rev. B 16 (1977) 1746-1747.

[5] L. Deng, F. Hu, M. Ma, S.C. Huang, Y. Xiong, H.Y. Chen, L. Li, S. Peng, Angew. Chem. Int. Ed. 60 (2021) 22276-22282.

[6] X. Ji, Y. Lin, J. Zeng, Z. Ren, Z. Lin, Y. Mu, Y. Qiu, J. Yu, Nat. Commun. 12 (2021) 1380.

[7] L. Guo, Q. Liu, Y. Liu, Z. Chen, Y. Jiang, H. Jin, T. Zhou, J. Yang, Y. Liu, Nano Energy. (2021) 106707.

[8] Y. Yang, K. Zhang, H. Lin, X. Li, H.C. Chan, L. Yang, Q. Gao, Adv. Funct. Mater. 29 (2019) 1805298.

[9] Q. Wang, H. Zhao, F. Li, W. She, X. Wang, L. Xu, H. Jiao, J. Mater. Chem. A 7 (2019) 7636-7643.

[10] F. Peng, L. Zhang, B. Jiang, H. Dou, M. Xu, N. Yang, J. Zhang, Y. Sun, Chem. Eng. J. 427 (2022) 131712.

[11] L. Dai, Z.N. Chen, L. Li, P. Yin, Z. Liu, H. Zhang, Adv. Mater. 32 (2020) 1906915.

[12] B. Chen, D. Kim, Z. Zhang, M. Lee, K. Yong, Chem. Eng. J. 422 (2021) 130533.

[13] Y. Yang, K. Zhang, H. Lin, X. Li, H.C. Chan, L. Yang, Q. Gao, ACS Catal. 7 (2017) 2357-2366.

[14] S. Ramakrishnan, J. Balamurugan, M. Vinothkannan, A.R. Kim, S. Sengodan, D.J. Yoo, Appl. Catal. B: Environ. 279 (2020) 119381.

[15] Y. Guo, J. Tang, J. Henzie, B. Jiang, W. Xia, T. Chen, Y. Bando, Y. Kang, M.S.A. Hossain, Y. Sugahara, Y. Yamauchi, ACS Nano 14 (2020) 4141-4152.

[16] P. Kuang, M. He, H. Zou, J. Yu, K. Fan, Appl. Catal. B: Environ. (2019) 15-25.

[17] B. Geng, F. Yan, L. Liu, C. Zhu, B. Li, Y. Chen, Chem. Eng. J. 46 (2021) 126815.